Journal of Applied Physics ARTICLE scitation.org/journal/jap

# Role of intrinsic defects on the persistent luminescence of pristine and Mn doped $ZnGa_2O_4$

Cite as: J. Appl. Phys. **125**, 095701 (2019); doi: 10.1063/1.5078773
Submitted: 29 October 2018 · Accepted: 17 February 2019 ·
Published Online: 1 March 2019

View Online Export Citation CrossMark

Yun-Peng Wang,[1] Hai-Shan Zhang,[1] Li-Ting Lin,[2] Shi-Feng Zhou,[2] Yao Yao,[1] Xiao-Bao Yang,[1] and Yu-Jun Zhao[1,a)]

## AFFILIATIONS

[1]Department of Physics, South China University of Technology, Guangzhou, Guangdong 510640, China
[2]School of Materials Science and Engineering, South China University of Technology, Guangzhou, Guangdong 510640, China

[a)]**Author to whom correspondence should be addressed:** zhaoyj@scut.edu.cn. **Tel.:** +86-20-87110426. **Fax:** +86-20-87112837.

## ABSTRACT

$ZnGa_2O_4$:Mn, as a distinct long persistent luminescence (PL) phosphor with green emission, has attracted intensive interest for display devices and security applications. We have systemically investigated the role of intrinsic defects in the PL of pristine and Mn doped $ZnGa_2O_4$ by first-principles calculations. It is found that the self-activated PL is attributed to the electron traps induced by $V_O$ and hole traps by $V_{Zn}$ and $Zn_{Ga}$. The doped Mn will be energetically favored at the tetrahedral sites rather than octahedral sites under an Mn-rich condition. In contrast, the site preference of Mn largely depends on the chemical potentials of Zn and Ga under Mn-poor condition. The existence of the antisite defect $Zn_{Ga}$, however, promotes the stability of Mn at octahedral sites significantly, forming corresponding defect complexes. The crystal field strength is significantly enhanced, while the spin splitting is reduced on Mn in the defect complex, which introduces additional near-infrared luminescence of PL as confirmed by our experiment.



## I. INTRODUCTION

Long persistent luminescence (PL) is a typical multifarious luminescence phenomenon that emissions in the visible and blue-green range can last for hours after the excitation.[1–3] Generally, it has been recognized that the electron traps store the excitation energy excited by the UV radiation or visible light and release it slowly to gain PL. The intrinsic defects or those intentionally introduced extrinsic defects, or both, yield the delayed luminescence.[4,5] This excellent PL property has huge application prospects, such as traffic signs, display devices, temperature sensors, security applications, and even in medical applications.[6]

In the middle of the 20th century, the first generation persistent phosphor ZnS:(Cu, Co) was proposed, though it is hard for practical application due to its poor brightness and lifetime, as reported in the literature.[7] Since Matsuzawa achieved a revolutionary persistent green-emitting phosphor $SrAl_2O_4$:Eu, Dy,[8] a flurry of new finds on optimal PL materials have been reported. Among various PL materials, a wide bandgap semiconductor, $ZnGa_2O_4$ (ZGO), has been singled out due to its self-activated blue light emitting and possible application on PL.[9]

The ternary compound oxide ZGO, composed of ZnO and $Ga_2O_3$, belongs to the spinel structures of $AB_2O_4$. For $AB_2O_4$ compounds, the divalent ion A usually fills in the tetrahedral void surrounded by four oxygen atoms, while the trivalent ions B occupy octahedral sites as shown in Fig. 1. However, exchanges of two types of ions in the lattice often occur, depending on the preparation method, experiment temperature, and chemical environment, possibly transforming a normal spinel into an inverse spinel.[10,11] It was reported that a weak inversion of spinel reaches approximately 3% in samples from a solid state method,[10] while Liu *et al.* prepared higher inversion samples of about 20% from a solgel method.[11] Due to the local electric field between two antisite defects (marked as $Zn_{Ga}^{-}$ and $Ga_{Zn}^{+}$) and the charge compensation effect, these defects often form antisite pairs. As a matter of fact, two emissions are often observed in pure ZGO, induced by the coupling of defect traps and electronic levels from Ga-O groups.[9,12] Jeong and Kim *et al.* ascribed the emissions to the distorted $[GaO_6]$ and $[GaO_4]$ structural units with oxygen vacancies, based on the binding energy difference by X-ray photoelectron spectroscopy (XPS) measurements.[12,13] Meanwhile, $V_O$ and $V_{Ca}$ are suggested to act as the electron and hole traps in PL of a similar phosphor, $CaAl_2O_4$:Eu.[14–16] It was also reported that many intrinsic defects are involved in PL, such as a blue emission of β-$Ga_2O_3$ and a green emission of ZnO.[17,18] Nevertheless, the

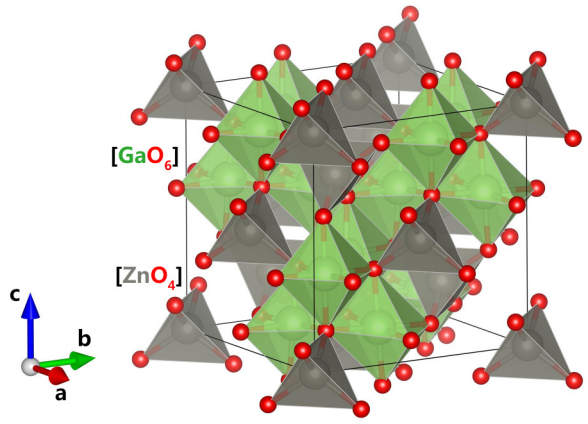


**FIG. 1.** The schematic spinel structure of ZGO: green for Ga, red for O, and gray for Zn.

role of intrinsic defects in the PL is not well understood, especially from the theoretical point of view.

While the normal ZGO phase is laborious to response in visible spectrum leading to poor PL property with a native large bandgap, color tuning has been realized in ZGO through doped $Mn^{2+}$, $Cr^{3+}$ ions, etc. and even co-doped with a variety of other ions.[19–21] The emission of PL is adjusted to green when Mn impurity is introduced, while it turns into red with Cr. It is critical to understand the role of these TMs (transition metals) in PL. De Vos *et al.* have reported that the local Cr environment will be severely distorted due to interactions of the $Zn_{Ga}$ antisite with the Cr atom.[21] Here, we choose to study $Mn^{2+}$ ion due to its broadband emission varying from green to deep red.[22] In fact, Mn could substitute either Ga or Zn atoms to form a stable local configuration in ZGO with different behaviors of PL, while the debate on the nature of substitution is still ongoing. Interestingly, the temperature and Mn-enrichment could affect the inversion parameter (the proportion of [$GaO_6$] and [$GaO_4$]).[10,23] Moreover, Liu *et al.* demonstrated that two antisite defects maintain a pretty high concentration by electron paramagnetic resonance (EPR) and XPS measurements. It is known to us that two types of crystal field environment will introduce two different emission bands resulting from $^4T_1$-$^6A_1$ transition of $Mn^{2+}$ ions.[24]

In this work, we have studied the impact of intrinsic defects on the PL property of self-activated and ZGO:Mn, via first-principles calculations. We find that defects of $V_O$, $V_{Zn}$, $Zn_{Ga}$, and $Ga_{Zn}$ have played critical roles in the self-activated PL property. Meanwhile, $Zn_{Ga}$ can promote Mn ions into octahedral sites to form [$MnO_6$] octahedron, even if the chemical environment changes. The binding energies reveal that defect $Zn_{Ga}$ or $V_{Zn}$ easily forms defect complex with doped Mn and has a remarkable influence on the PL property.

## II. COMPUTATIONAL DETAILS

We perform the first-principles calculations based on the density functional theory (DFT) method by using the Vienna *ab initio* simulation package (VASP) code.[25,26] The projector augmented wave (PAW) method with generalized gradient approximation (GGA) of the Perdew-Burke-Ernzerhof (PBE) functional was employed for describing the exchange correlation potential.[27,28] To meet with maximum experimental doping concentration (0.5%–5%) in ZGO:Mn as far as possible,[10,23] we adopt the $2\times2\times2$ supercell for understanding the defect property in the host material. The cutoff energy of a plane-wave basis set was set as 700 eV. All the structures are fully relaxed with a mesh of $1\times3\times3$ obtained by the Monkhorst-Pack method,[29] and the force criterion is 0.02 eV/Å. The DFT-1/2 method is adopted to obtain more accurate bandgaps with respect to the conventional gap-underestimation functional, where the DFT-1/2 method shows a typical behavior that the eigenvalues and the bandgap are exhibited as a trimming function of self-energy potential defined in the atoms, as bandgaps frequently depend on specific atoms and bonding types for a given semiconductor.[30] The optimal parameter *CUT* of this function makes the bandgap extreme, as is the case of an ionic or covalent radius. On the other hand, considering the primary contribution to valence band maximum (VBM), the optimal values of *CUT* were selected to O *p* orbital (2.67), Ga *d* orbital (1.23), and Zn *d* orbital (1.67) (see Table S1 in the supplementary material), which are consistent with the radius cutoff for calculations of subsequent partial density of states (PDOSs). The DFT-1/2 method is demonstrated to provide a reasonable bandgap of ZGO compared with experimental values (~4.4 eV), with the same computational cost as the standard DFT.[30–32]

We have calculated the formation energies of all the possible intrinsic defects using the following equation:[33,34]

$$\Delta H_f^{(\alpha,q)} = E_D(\alpha, q) - E_P(0) + \sum_i n_i(\Delta\mu_i + \mu_i^{solid}) + q(E_{VBM} + E_F + \Delta V). \quad (1)$$

Here, $E_D(\alpha,q)$ and $E_P(0)$ are the total energies of supercells with and without defect $\alpha$; $\Delta\mu_i$ is the atom chemical potential of constitute $i$ referred to its most stable phase with energy $\mu_i^{solid}$; $n_i$ is the number of each element; $q$ represents the charge state of defect $\alpha$; $E_{VBM}$ is referenced to VBM of the defect free system; and $E_F$ is the Fermi level relative to the $E_{VBM}$. The potential alignment correction term $\Delta V$ is added to align the VBM energy in systems with different charged states[35] and is referenced to local atomic electrostatic potentials farther away from the defect site between the neutral and charged defects. In terms of greater simulated doping concentration than an experiment, the total energy of charged defects in a supercell, $E_D(\alpha,q)$, is corrected up to the quadrupole term according to the Makov-Payne scheme to overcome the image charge interaction from periodic boundary condition.[36]

## III. EXPERIMENT DETAILS

Preparation: The pure and 1% $Mn^{2+}$ doped ZGO phosphors were prepared via the traditional high temperature solid state reaction.[22] The high purity ZnO (99.95%), $Ga_2O_3$ (99.999%), and $MnCO_3$ (AR) raw materials were weighed according to the nominal compositions. In a typical synthesis, stoichiometric mixtures of the raw powders were ground in an agate mortar for 0.5 h without ethanol

to ensure homogeneity. The mixtures of composition were calcined in the aluminum oxide crucible at about 1300 °C for 2 h. After the system cooled to room temperature naturally, the production was reground for the following photoluminescence characterization.

Characterization methods: Static excitation and emission spectra were recorded on an FLS920 spectrofluorometer (Edinburgh Instruments) in single photon counting mode.

## IV. RESULTS AND DISCUSSION

### A. Electronic structure of pristine ZGO

The band structure and the PDOS of the pristine ZGO are calculated by GGA and DFT-1/2 methods, respectively, as shown in Fig. 2. The VBM of ZGO appears along the K-Γ direction, while the conduction band maximum (CBM) is located exactly at the Γ point, indicating the nature of an indirect bandgap semiconductor. The crystal structure of ZGO mainly consists of [$ZnO_4$] tetrahedron and [$GaO_6$] octahedron. Hence, the bonding orbitals of Zn-O and Ga-O groups mainly contribute to the valence and the conduction band. The corresponding PDOS reveals that the VBM is primarily contributed from O 2*p*, Ga 3*d*, and Zn 3*d* levels, whereas the CBM mainly originates from Ga 4*s* and O 2*p* levels, forming a dispersed band. The calculated bandgap is only 2.29 eV due to the well-known limitation of GGA-PBE in predicting the bandgaps in a strongly correlated system, which is dramatically narrower than the experimental value, ~4.4 eV.

To improve the bandgap evaluation, the DFT-1/2 method with no remarkable additional computational effort is also employed. From Fig. 2(b), we could observe that DFT-1/2 gives similar dispersion relations as GGA-PBE on band structure but with the much improved bandgap. In this case, the self-energy potential does not cause significant band deformation and reserves the nature of indirect bandgap. In order to analyze the difference between two dispersed bands in deep insight, we also calculated the effective mass of conduction band, which turns to be 1.01 e and 1.28 e from GGA and DFT-1/2 calculations, respectively, in line with the results in the literature.[37,38]

### B. Intrinsic defects and self-activated PL

#### 1. Phase diagram and defect formation energy

In order to sustain the existence of stable pure phase ZGO and avoid the formation of competing for secondary compounds (such as elementary substances, ZnO and β-$Ga_2O_3$, as well as the impurity involved phase $Mn_3O_4$), the chemical potential $\mu_i$ should be satisfied with the following constraints:

$$\Delta\mu_{Zn} \le 0,\ \Delta\mu_{Ga} \le 0,\ \Delta\mu_{O} \le 0,\ \Delta\mu_{Mn} \le 0, \tag{2}$$

$$\Delta\mu_{Zn} + 2\Delta\mu_{Ga} + 4\Delta\mu_{O} = \Delta H_f(ZnGa_2O_4), \tag{3}$$

$$\Delta\mu_{Zn} + \Delta\mu_{O} \le \Delta H_f(ZnO), \tag{4}$$

$$2\Delta\mu_{Ga} + 3\Delta\mu_{O} \le \Delta H_f(Ga_2O_3), \tag{5}$$

$$3\Delta\mu_{Mn} + 4\Delta\mu_{O} \le \Delta H_f(Mn_3O_4). \tag{6}$$

The calculated chemical potential region of Zn, Ga, and O is shown in Fig. 3(a), with only the narrow area of A–B–C–D–E (includes blue and orange areas) available for the stable ZGO. On the other hand, the wide range of the oxygen chemical potential provides the possible flexibility to tune the concentration of intrinsic defects by controlling the growth conditions. Herein, we have selected five typical chemical potential points (A, B, C, D, and E) on the boundary of phase diagram and one point (F) at the centre to investigate the formation of various defects.

We have plotted the formation energies of various single defects as a function of $\Delta\mu_O$ in Fig. 3(b). Here, the neutral acceptor defects of $V_{Zn}$, $Zn_{Ga}$ are pinned around the VBM, while the neutral donor defects of $V_O$, $Ga_{Zn}$ are available around the CBM. The formation energies of these defects can be tuned in a large range due to the relative broad choice of oxygen potential in the stable region of ZGO [cf. Fig. 3(a)]. The lowest formation energy of $Ga_{Zn}$ defect increases [see Fig. 3(b)], while that of $Zn_{Ga}$ decreases as $\mu_O$ moves from O-poor to O-rich and vice versa. It is noticed that the fairly low formation energies of $V_O$ and $V_{Zn}$ are in analogy with the spinel $CaAl_2O_4$, where both O and Ca vacancies are easy to form.[17–19] The other intrinsic defects ($V_{Ga}$, $Ga_O$, $Zn_O$, $O_{Zn}$, $O_{Ga}$, and $O_i$) will not be considered due to their high formation energies.

#### 2. Transition energy level and self-activated PL property

We have learned that two antisite defects, $Ga_{Zn}$ and $Zn_{Ga}$, and two vacancy defects, $V_O$ and $V_{Zn}$, are the most energetically favored

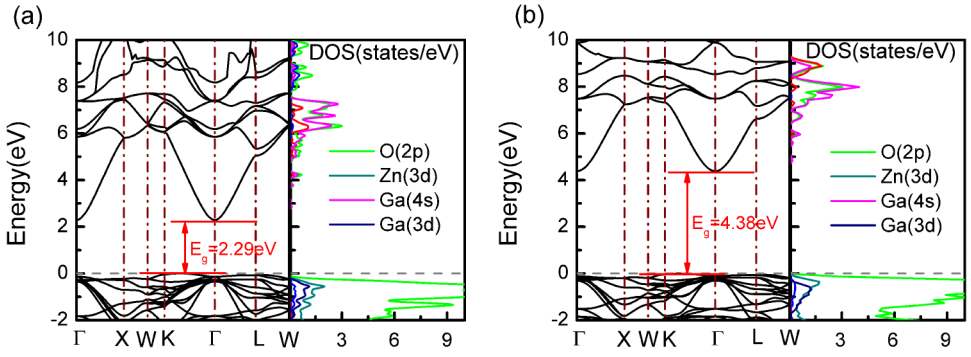


**FIG. 2.** Calculated electronic band structure and partial density of states (PDOSs) of the pristine ZGO by (a) the GGA-PBE method and (b) the DFT-1/2 method. The VBM is set to zero.

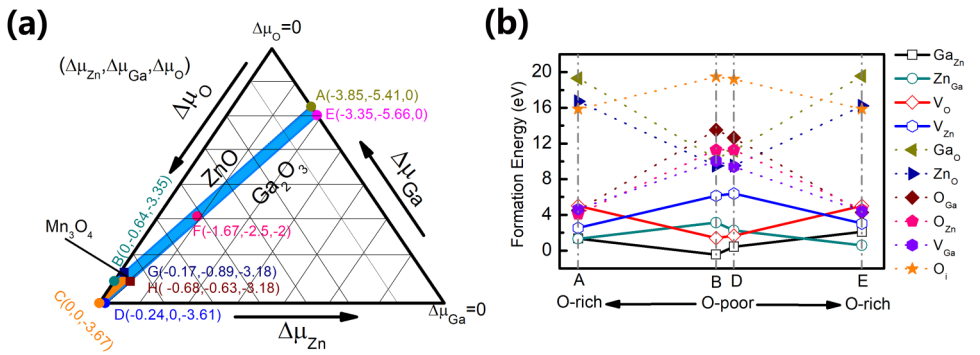


**FIG. 3.** (a) Thermodynamic stable range of chemical potential region (pristine ZGO in blue and doped ZGO: Mn in orange) for equilibrium growth. (b) Calculated formation energy of defects as a function of the chemical potential, as $\mu_O$ moves along the A–B–D–E line. The open symbols denote dominant defects, while the solid ones correspond to defects with relative high formation energies.

intrinsic defects. Their defect transition energy levels $\varepsilon_\alpha(q/q')$ correspond to the Fermi level position where two different charged defect states have the same formation energy, i.e., $\Delta H^{(\alpha,q)} = \Delta H^{(\alpha,q')}$.[39]

In Fig. 4, the calculated formation energies and transition energy levels at three typical chemical potential points are shown. The formation energies of charged defects also have a relatively large variation as for a wide gap semiconductor. On the donor-defect side, $Ga_{Zn}$ has a resonant electron trap level inside the conduction bands, meaning that neutral $Ga_{Zn}$ is easy to release an electron into the conduction band, and shifting to the charge state of 1+. Slightly different from $Ga_{Zn}$, $V_O$ will generate one thermodynamic stable transition energy level ε(+2/0) at $E_F = 3.49$ eV, indicating that there are two electrons released or trapped at each oxygen vacancy defect level. Unlike donor defects, each $Zn_{Ga}$ ($V_{Zn}$) creates a relative shallow energy level of 0.87 eV (0.35 eV) near the VBM. These two empty impurity levels can accommodate electrons or holes as a carrier reservoir. Under the O-poor condition, the donors have higher concentrations, leading to the pinned Fermi level closer to the CBM. As the chemical potential changes, $Zn_{Ga}$ gradually becomes the dominant defect to offset the effect on the Fermi level influenced by the donor defects, shifting $E_F$ to the middle position. Therefore, the pinned Fermi levels can be widely tuned by the chemical environment. The pinned Fermi level is capable of qualitatively reflecting the charge state of every defect and affecting the transition of electrons. Here, we have observed that the charge states of $V_{Zn}$, $Zn_{Ga}$, and $Ga_{Zn}$ will stay at 2−, 1−, and 1+ in the tunable Fermi energy range, while $V_O$ will vary from 2+ to neutral. The charge state variation of oxygen vacancy was also reported in the literature.[13]

The calculated impurity levels from the DFT-1/2 method are expected to qualitatively reflect the transition levels of the corresponding defects. As shown in Fig. 5(a), ZGO with $Zn_{Ga}$ ($V_{Zn}$) introduces pretty shallow impurity levels above VBM, in line with the calculated transition levels in Fig. 4. As for donor defects, $V_O$ introduces defect levels in the middle of bandgap, usually acting as energy storage for long PL.[16] However, $Ga_{Zn}$ defect introduces no level inside the gap but inside the conduction band. We also notice that the O 2*p* level has contributions to all the impurity levels in the gap, due to dangling bonds and antisite bonds corresponding to the defect configuration.

Furthermore, we have calculated the absorption spectrum of bulk ZGO without and with defects, as shown in Fig. 5(b). The absorption spectrum of ZGO with defects is similar to that of pristine ZGO for absorption energy greater than 4.4 eV, illustrating

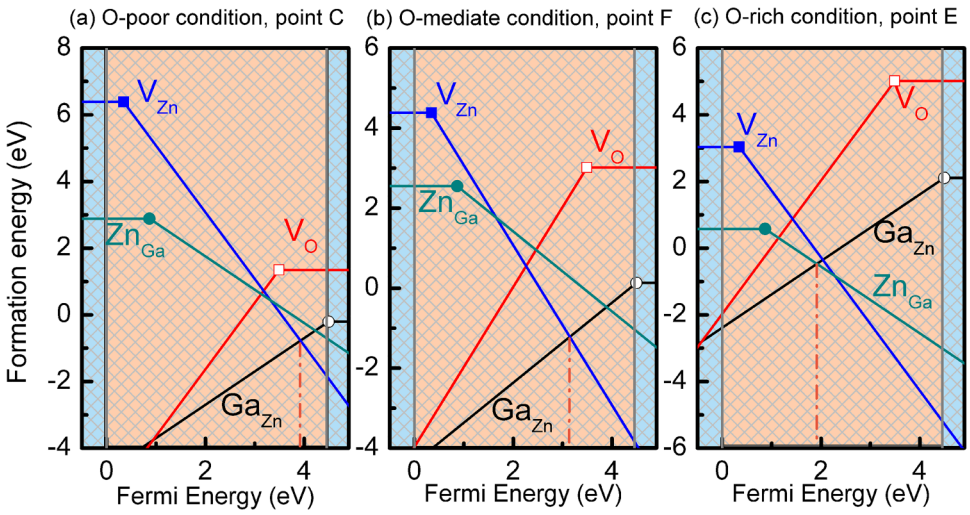


**FIG. 4.** The formation energies of intrinsic defects in ZGO under a different oxygen environment, points C (a), F (b), and E (c) as O-poor, O-mediate, and O-rich regions, respectively [cf. Fig. 3(a)]. Only the four dominant defects with low formation energies are illustrated, with the vertical dashed lines representing the pinned Fermi levels.

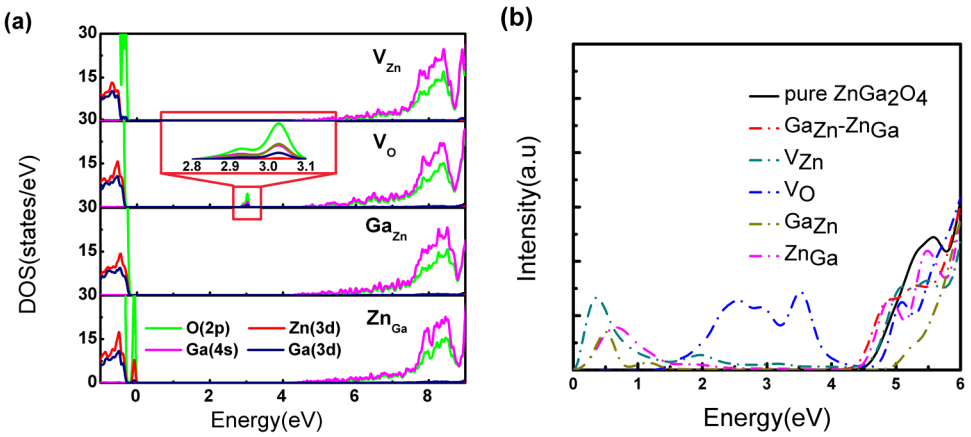


**FIG. 5.** (a) Calculated PDOS of ZGO with isolated $V_{Zn}$, $V_O$, $Ga_{Zn}$, and $Zn_{Ga}$ defects. (b) Calculated absorption spectrum of pristine ZGO and with various single defects (such as $Ga_{Zn}$, $Zn_{Ga}$, $V_O$, and $V_{Zn}$).

that intrinsic defects have no remarkable changes on the bandgap of bulk ZGO. It is observed in the absorption spectrum that two peaks around the energy of 0.4 eV and 0.7 eV emerge above the VBM induced by $Zn_{Ga}$ and $V_{Zn}$, in line with their transition levels, 0.35 and 0.87 eV, respectively. The peaks just above 0 eV of the spectrum of ZGO:$Ga_{Zn}$ are attributed to the initial emission of electrons from neutral $Ga_{Zn}$ defects, which is adopted in our calculation of absorption spectrum. Of note, the calculated spectrum of ZGO:$Ga^{+}_{Zn}$ system will be identical to that of pristine ZGO as $Ga_{Zn}$ has a resonance defect level inside the conduction band (see Fig. 4). Moreover, unionized $V_O$ preferentially releases two electrons to introduce two peaks similar to $Ga_{Zn}$. Subsequently, electrons from VBM are excited to the ionized level of $V^{2+}_O$ about 3.49 eV. There are no significant peaks observed in ZGO:($Ga_{Zn}$, $Zn_{Ga}$), mainly due to the charge compensation effect between $Ga^{+}_{Zn}$ and $Zn^{-}_{Ga}$, implying that the defect complex contributes little to the self-activated PL.

The wide bandgap semiconductor generally has a poor efficiency on PL property. The reported blue emission of β-$Ga_2O_3$ and green emission of ZnO are largely due to a strong correlation between luminescence intensity and the formation of intrinsic defects, as suggested by Onuma *et al.*[17] and Sambandam *et al.*[18] As for two self-activated emissions, a superposition of broad peak around 400–480 nm has been observed in pristine ZGO prepared in an oxidation environment. However, the above broad peak disappears and only one main peak of luminescent emission is observed around 360 nm of pristine ZGO in a reduction environment.[12] It is also reported that the $V_O$ defect could give rise to the emission phenomenon.[9] Following the above qualitative analysis and experiment observation, we construct a feasible model to explain these two self-activated emissions. When the ZGO samples prepared under an O-rich condition, i.e., the oxidation environment, $V_O$ is energetically favored at the 2+ charge state, and the neutral $Zn_{Ga}$ will act as hole traps, as well as neutral $V_{Zn}$. According to our calculation, the energy difference between the transition level of $V^{2+}_O$ and the levels of $V^{0}_{Zn}$ and $Zn^{0}_{Ga}$ is 3.14 and 2.62 eV, respectively. The calculated transition energies are in good agreement with the reported blue emission in the oxidation environment. In addition, ZGO tends to exhibit n-type conductivity under the O-poor condition corresponding to the reduction environment, maintaining a high Fermi level, so that the impurity level of $V_O$ will hold on the unionized state mostly. When electrons are excited to CBM by UV radiation and return back to VBM, they skip the electron-occupied $V_O$ impurity level and directly transmitted to the $Zn_{Ga}$ impurity level with an emission around 360 nm. Actually, the calculated thermodynamic transition levels between the fully relaxed defect structures are in line with the optical levels within a minor difference.[40,41]

### C. Influence of intrinsic defects on the stability and PL property of Mn impurity

#### *1. Site preference of Mn impurity*

Experimentally, Mn ions can emit green or red luminescence in ZGO excited by UV radiation.[10,23] Considering the close ionic radii and possible oxidation state around 2+ to 3+, Mn dopant induces two kinds of substitutions $Mn_{oct}$ and $Mn_{tet}$ in the ZGO system. In fact, under low concentration of Mn dopant, i.e., the Mn-poor condition, we find that Mn could be stabilized at both tetrahedral and octahedral sites in pristine ZGO as the oxygen chemical potential tunes in a large range (see Fig. S1 in the supplementary material). When Mn is heavily doped, the tetrahedral site is energetically favored for Mn in pristine ZGO, as the chemical potentials of O, Zn, and Ga are limited in a small range [cf. Fig. 3(a)] under an equilibrium condition.

It is known that antisite defects ($Ga_{Zn}$ and $Zn_{Ga}$) have low formation energies at the pinned Fermi level from Fig. 4, indicating a high concentration in the ZGO, in line with the experimental observation.[10] In Fig. 6, we illustrate the doping process of Mn with and without the antisite defects. Under the Mn-rich environment, Mn atoms prefer the tetrahedral sites than octahedral sites energetically without the pre-existed antisite defects. Therefore, in terms of thermodynamic state, the stability of [$MnO_4$] octahedron prevails to [$MnO_6$]. Interestingly, it is known that the antisite defect could be largely available up to about 20% in ZGO samples prepared from the solgel method.[11] According to our calculation, Mn atoms will be much easier to substitute Zn atoms at octahedral sites with the pre-existed antisite $Zn_{Ga}$, though it is hard for Mn directly

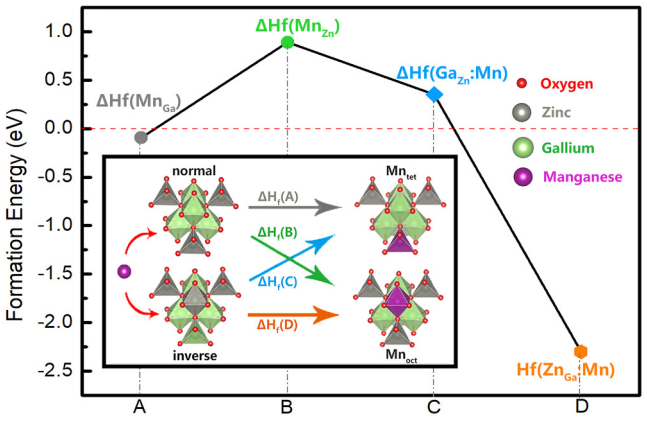


**FIG. 6.** Schematic diagram of four possible ways to form two types of Mn dopant and their respective formation energies under the Mn-rich environment.

entering into octahedral sites. For the inclusion of $Ga_{Zn}$, it has a slight influence on [$MnO_4$] tetrahedron. Therefore, we speculate that Mn atoms could also substitute Zn atoms at Ga sites to form $Mn_{oct}$ as well as $Mn_{tet}$ due to the matched charge state, as we know that the location of $Mn^{2+}$ is related to temperature in the literature.[23] This result could explain why Mn atoms could occupy either octahedral sites or tetrahedral sites with the variation of antisite concentration.[10] For Mn dopant, the comparison among four possible ways to form two types of Mn substitutions can provide a useful guidance for experiments.

### 2. The optical property of ZGO:Mn without and with defect complex

Although $Zn_{Ga}$ could affect the site preference of Mn impurity, $Mn_{tet}$ is still dominated than $Mn_{oct}$. We, therefore, attempt to associate the $^4T_1$-$^6A_1$ transition to our calculated electronic structures of $Mn_{tet}$ with and without Mn defect complex, based on the model of $Mn_{tet}$. The electronic structures of Mn-doped ZGO are shown in Fig. 7(a). In comparison with the PDOS and band structure of pristine ZGO [Fig. 2(a)], we find that the doped Mn introduces impurity levels into the bandgap. Both PDOS and band structure indicate that the Mn 3*d* levels exhibit a large spin split due to the strong exchange interaction. The introduced impurity levels are divided into two parts: the electron-occupied part is located 2 to 2.55 eV above the VBM and the unoccupied part is located 1.7 eV above the CBM. The calculated energy difference between the 3*d* majority and minority spin levels of Mn is approximately 3.7-4.25 eV, much greater than the theoretical evaluation of the transition from $^6S$ to $^4G$ (~3.3 eV), according to Tanabe-Sugano diagram,[42] and the experiment emission peak of 2.0–3 eV (420–620 nm).[3,23,43] The $^6S$ ground state level is corresponding to the fully occupied $t_2$ and $e$ in the majority spin channel. When electrons are excited to higher levels by UV radiation, configuration $^4L$ could be formed, and energy will be released as the electrons tend to relax to the ground state. As we know, the crystal-field effect propels the $^4G$ level (the lowest one of $^4L$ configurations) to further split into $^4E$, $^4A_1$, $^4T_1$, and $^4T_2$. Here, we obtain the Dq (crystal field strength, which equals to 9/40 of the *e*, $t_2$ splitting energy difference in the tetrahedral configuration[44]) to be ~0.12 eV, similar with an experiment value.[45]

Experiment results in Fig. 7(b) show that pristine ZGO has a near infrared emission of 1270 nm after excitation at 250 nm, while ZGO:Mn also possesses a near infrared emission band around 1100 nm under excitation of 275 nm. Furthermore, ZGO:Mn samples exhibit an additional excitation peak at 475 nm by monitoring the emission at 1110 nm. The notable contrast in the emission and excitation feature between ZGO and ZGO:Mn indicates that the near infrared emission of 1100 nm is ascribed to Mn dopant. However, the origin of near infrared luminescence still needs to be further investigated. In fact, we find in the following discussion that $Mn_{tet}$ can easily form a defect complex with a greater Dq value, which might contribute to the near infrared luminescence mentioned above.

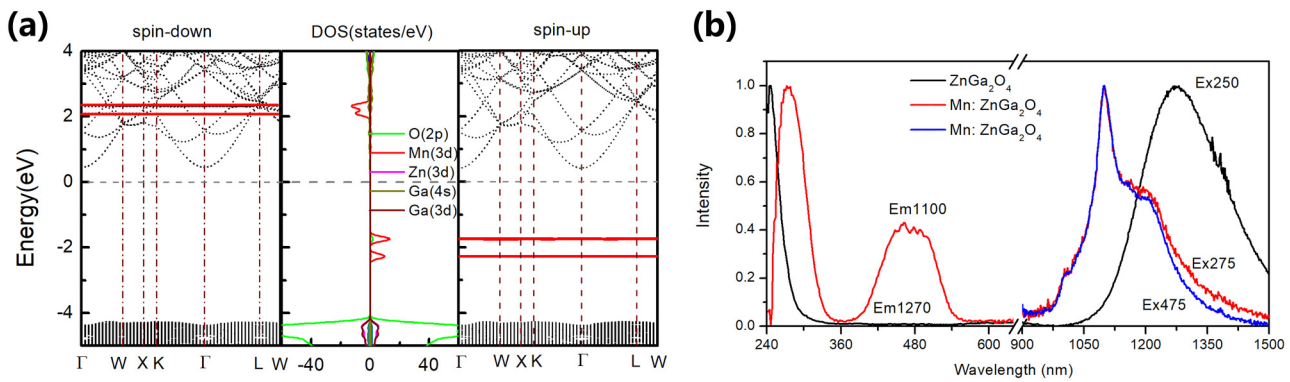


**FIG. 7.** (a) DFT-1/2 calculated band structures and PDOSs of ZGO: $Mn_{Zn}$. Mn 3*d* levels are denoted by the red solid lines in the band structure and PDOS. The pinned energy level (see Fig. S2 in the supplementary material) is set to zero. (b) Photoluminescence excitation and emission spectra of ZGO without Mn dopant and with Mn dopant from the experiment.

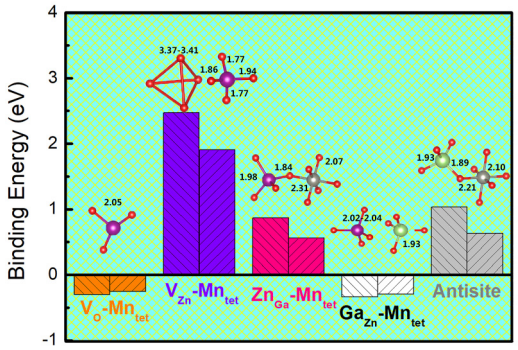


**FIG. 8.** Calculated binding energies of various defect complexes (left column, nearest neighbor) vs the distanced defect combination (furthest distance in the supercell). Here, the corresponding bond lengths of local structure configuration of the fully relaxed defect complex are also given.

As the intrinsic defects play an important role in self-activated PL, here, we further study the influence of intrinsic defects on a ZGO:$Mn^{2+}$ PL property, focusing on the $Mn_{tet}$ contained defect complex. The stability of the defect complex is determined by its binding energy, which is defined by

$$E_b = \Delta H_f(\mathrm{Mn_{tet}}) + \Delta H_f(X) - \Delta H_f(\mathrm{Mn_{tet}} + X), \quad (7)$$

where $\Delta H_f(X)$ is the formation energy of the single defect $X$ (including $V_O$, $V_{Zn}$, $Ga_{Zn}$, and $Zn_{Ga}$). For complexes ($Mn_{tet}$, $X$), we consider four possible models, even considering the antisite pair as a comparison as shown in Fig. 8. For ($V_{Zn}$, $Mn_{tet}$) and ($Zn_{Ga}$, $Mn_{tet}$), their positive binding energies indicate that it is energetically favored for the sample containing both ($Mn_{tet}$, $V_{Zn}$) and ($Mn_{tet}$, $Zn_{Ga}$), as well as the antisite pair. The greater $E_b$ of ($Mn_{tet}$, $V_{Zn}$) stands for a stronger interaction within the complex than that of ($Mn_{tet}$, $Zn_{Ga}$). However, the defect complexes of ($V_O$, $Mn_{tet}$) and ($Ga_{Zn}$, $Mn_{tet}$) are hard to form due to their negative binding energy, which mainly attributes to the electrostatic repulse between the complex components. We also compare the binding energies of the defect complexes with their corresponding combinations with the furthest distance in the given supercell (cf. Fig. 8). The comparison shows that the nearest combinations are remarkably more stable than the distanced combination, indicating the stability of the $Mn_{tet}$ defect complexes.

A series of local atomic structures of fully relaxed defect complexes are shown in Fig. 8. When Ga and Zn atoms exchange their position, the bond length of [$GaO_4$] tetrahedron and [$ZnO_6$] octahedron is 1.93 and 2.08 Å differing from original Ga–O and Zn–O bond lengths of 2.02 and 2.00 Å. The bond length of [$MnO_4$] tetrahedron is 2.03 Å, which is close to that of the Zn–O bond (see Table S2 in the supplementary material). We notice that the distance of Mn–O nearly has no remarkable change when forming defect complex with $V_O$ or $Ga_{Zn}$. In contrast, $V_{Zn}$ and $Zn_{Ga}$ introduce an obvious distortion for [$MnO_4$] tetrahedron, which is expected to attribute to a large Coulomb interaction between the defects.

According to the above calculations, defect complexes of ($Mn_{tet}$, $V_{Zn}$) and ($Mn_{tet}$, $Zn_{Ga}$) are largely available in ZGO:Mn. To shed light on the influence of the defect complex to the PL properties of ZGO:Mn, we have compared the electronic structures of ZGO with single $Mn_{tet}$ defects and defect complexes of ($Mn_{tet}$, $V_{Zn}$) or ($Mn_{tet}$, $Zn_{Ga}$). According to Fig. 8(b), Mn 3*d* levels keep away from the VBM due to the formation of the defect complexes. Furthermore, the previous induced levels are further degenerated, with both the majority and minority spin levels above VBM, as shown in Fig. 9. The splitting levels can be attributed to the charge transfer between the defect complexes.[21] Moreover, the minority spin levels move down and are located just below the CBM, while the majority spin levels are close to CBM. The energy difference in spin splitting between $^6S$ and $^4G$ further decreases to 3-3.8 and 2.2-3.4 eV, respectively. For the $Mn_{tet}$ with hole-type trap nearby, we speculate that electrons from VBM excited by UV light can easily move to the empty minority spin 3*d* levels than without hole-type trap nearby.

As shown in Fig. 8, the Mn–O bond length shrinks by 0.15 and 0.2 Å on average, indicating a stronger crystal field effect of Mn–O interplay. The calculated Dq has increased to a greater value of about 0.20 and 0.22 eV correspondingly. The decreased energy

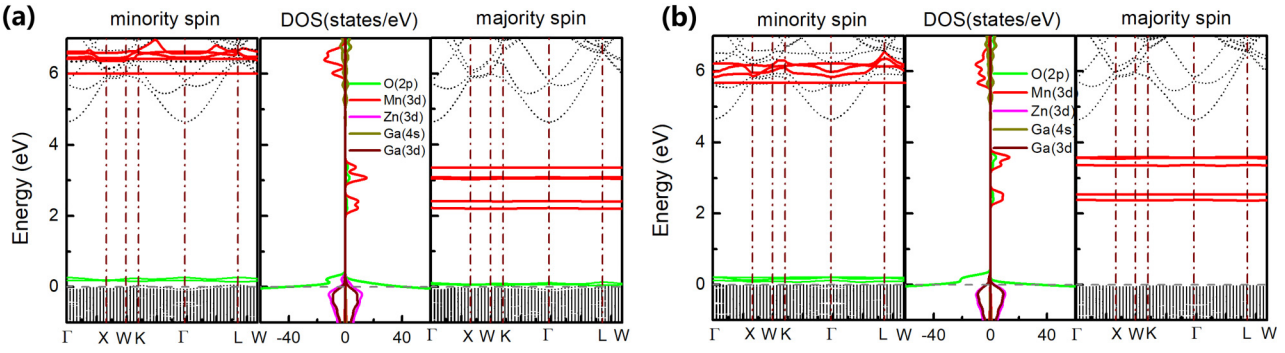


**FIG. 9.** DFT-1/2 calculated band structures and PDOSs of ZGO with defect complexes of (a) ($Zn_{Ga}$, $Mn_{tet}$) and (b) ($V_{Zn}$, $Mn_{tet}$). Mn 3*d* levels are denoted by the red solid lines in the band structures and PDOSs, while the green solid lines for $V_{Zn}$ (the dangling bonds of corresponding oxygen ions) and $Zn_{Ga}$ defects. The VBM is set to zero.

difference and enhanced Dq imply that ZGO:Mn with hole-type traps nearby will induce a near infrared luminescence according to the Tanabe-Sugano diagram, theoretically. It could explain why the additional near-infrared luminescence emerges in ZGO:Mn, as shown in Fig. 7(b). Furthermore, high density of $V_{Zn}$ and $Zn_{Ga}$ would be harmful as they are highly likely to transform the valence state of Mn ions from +2 to higher-valence states.

## V. CONCLUSION

In summary, we have theoretically investigated the defect stability and PL property of intrinsic defects and extrinsic defects for ZGO. The theoretical simulation shows that the self-activated persistent luminescence is caused by the electron traps induced by $V_O$, $V_{Zn}$, and $Zn_{Ga}$ in pristine ZGO. The doped Mn ions prefer to replace Zn in ZGO, and $Mn_{oct}$ will be favored with the existence of $Zn_{Ga}$. With the company of $V_{Zn}$ and $Zn_{Ga}$, the near infrared luminescence of Mn doped ZGO is predicted by our theoretical calculations and confirmed by experiment subsequently. Our comprehensive study of PL property of pristine and Mn doped ZGO provides an insight into the tunable PL property of ZGO, helpful for further development of defect-controllable luminescence materials.

## SUPPLEMENTARY MATERIAL

See the supplementary material for additional information on optimal values of *CUT*, formation energies, and structure parameters.

## ACKNOWLEDGMENTS

This work is financially supported by the NSF of China (NSFC) (Grant Nos. 11574088 and 51431001), the Foundation for Innovative Research Groups of the National Natural Science Foundation of China (NNSFC) (Grant No. 51621001), and the Natural Science Foundation of Guangdong Province of China (Grant No. 2016A030312011).

## REFERENCES

[1]Y. Li, S. F. Zhou, Y. Y. Li, K. Sharafudeen, Z. J. Ma, G. P. Dong, M. Y. Peng, and J. R. Qiu, J. Mater. Chem. C **2**, 2657–2663 (2014).
[2]P. F. Li, M. Y. Peng, L. Wondraczek, Y. Q. Zhao, and B. Viana, J. Mater. Chem. C **3**, 3406–3415 (2015).
[3]J. Qian, P. F. Li, Y. F. Huang, C. W. Wang, Y. Zhang, F. Bai, W. Z. Fan, Y. B. Li, H. J. Li, M. Peng, Y. Dai, and Q. Z. Zhao, Opt. Mater. Express **6**, 2380–2388 (2016).
[4]T. Aitasalo, J. Hölsä, H. Jungner, M. Lastusaari, and J. Niittykoski, J Phys. Chem. B **110**, 4589–4598 (2006).
[5]P. Dorenbos, Phys. Status Solidi B **242**, R7–R9 (2005).
[6]J. Botterman and P. F. Smet, Opt. Express **23**, A868 (2015).
[7]W. Hoogenstraaten and H. A. Klasens, J. Electrochem. Soc. **100**, 366–375 (1953).
[8]T. Matsuzawa, J. Electrochem. Soc. **143**, 2670–2673 (1996).
[9]I. K. Jeong, H. L. Parkb, and S. I. Mho, Solid State Commun. **105**, 179–183 (1998).
[10]M. Allix, S. Chenu, E. Véron, T. Poumeyrol, E. A. Kouadri-Boudjelthia, S. Alahraché, F. Porcher, D. Massiot, and F. Fayon, Chem. Mater. **25**, 1600–1606 (2013).
[11]J. Liu, X. L. Duan, Y. Zhang, and H. D. Jiang, J. Phys. Chem. Solids **81**, 15–19 (2015).
[12]J. S. Kim, H. I. Kang, W. N. Kim, J. I. Kim, J. C. Choi, H. L. Park, G. C. Kim, T. W. Kim, Y. H. Hwang, S. I. Mho, M. C. Jung, and M. Han, Appl. Phys. Lett. **82**, 2029–2031 (2003).
[13]C. Satya Kamal, S. Boddu, B. Vishwanadh, K. R. Rao, V. Sudarsan, and R. K. Vatsa, J. Lumin. **188**, 429–435 (2017).
[14]P. Dorenbos, J. Electrochem. Soc. **152**, H107 (2005).
[15]X. H. Xu, X. Yu, D. C. Zhou, and J. B. Qiu, Mater. Res. Bull. **48**, 2390–2392 (2013).
[16]B. Y. Qu, B. Zhang, L. Wang, R. L. Zhou, and X. C. Zeng, Chem. Mater. **27**, 2195–2202 (2015).
[17]T. Onuma, S. Fujioka, T. Yamaguchi, M. Higashiwaki, K. Sasaki, T. Masui, and T. Honda, Appl. Phys. Lett. **103**, 041910 (2013).
[18]B. Sambandam, R. J. Michael, and P. T. Manoharan, Nanoscale **7**, 13935–13942 (2015).
[19]J. H. Cha and H. W. Choi, Trans. Electr. Electron. Mater. **12**, 11–15 (2011).
[20]Y. X. Zhuang, J. Ueda, and S. Tanabe, Appl. Phys. Express **6**, 052602 (2013).
[21]A. De Vos, K. Lejaeghere, D. E. Vanpoucke, J. J. Joos, P. F. Smet, and K. Hemelsoet, Inorg. Chem. **55**, 2402–2412 (2016).
[22]X. Y. Sun, Z. He, and X. Gu, J. Mater. Sci. Mater. Electron. **29**, 17217–17221 (2018).
[23]J. S. Kim, J. S. Kim, T. W. Kim, S. M. Kim, and H. L. Park, Appl. Phys. Lett. **86**, 091912 (2005).
[24]G. K. B. Costa, S. S. Pedro, I. C. S. Carvalho, and L. P. Sosman, Opt. Mater. **31**, 1620–1627 (2009).
[25]G. Kresse and J. Furthmuller, Phys. Rev. B **54**, 11169 (1996).
[26]D. J. G. Kresse, Phys. Rev. B **59**, 1758 (1999).
[27]P. E. Blöchl, Phys. Rev. B **50**, 17953–17979 (1994).
[28]J. P. Perdew and M. E. Kieron Burke, Phys. Rev. Lett. **77**, 3865 (1996).
[29]H. J. Monkhorst and J. D. Pack, Phys. Rev. B **13**, 5188–5192 (1976).
[30]L. G. Ferreira, M. Marques, and L. K. Teles, Phys. Rev. B **78**, 125116 (2008).
[31]T. Omata, N. Ueda, K. Ueda, and H. Kawazoe, Appl. Phys. Lett. **64**, 1077–1078 (1994).
[32]Q. Shi, J. Y. Zhang, C. Cai, L. Cong, and T. M. Wang, Mater. Sci. Eng. B **149**, 82–86 (2008).
[33]S. B. Zhang, S. H. Wei, and A. Zunger, Phys. Rev. B **63**, 075205 (2001).
[34]S. H. Wei and S. B. Zhang, Phys. Rev. B **66**, 155211 (2002).
[35]T. Mattila and A. Zunger, Phys. Rev. B **58**, 1367–1373 (1998).
[36]G. Makov and M. C. Payne, Phys. Rev. B **51**, 4014–4022 (1995).
[37]S. C. Yan, J. J. Wang, H. L. Gao, N. Y. Wang, H. Yu, Z. S. Li, Y. Zhou, and Z. G. Zou, Adv. Funct. Mater. **23**, 758–763 (2013).
[38]Y. G. Xia, T. Wang, X. Z. Zhao, X. L. Jiao, and D. R. Chen, J. Phys. Chem. C **122**, 5509–5517 (2018).
[39]S. H. Wei, Comp. Mater. Sci. **30**, 337–348 (2004).
[40]J. B. Varley, A. Janotti, C. Franchini, and C. G. Van de Walle, Phys. Rev. B **85**, 081109 (2012).
[41]J. Dressel, M. Malik, F. M. Miatto, A. N. Jordan, and R. W. Boyd, Rev. Mod. Phys. **86**, 307–316 (2014).
[42]Y. Tanabe and S. Sugano, J. Phys. Soc. Jpn. **9**, 766–779 (1954).
[43]K. Somasundaram, K. P. Abhilash, V. Sudarsan, P. Christopher Selvin, and R. M. Kadam, Phys. B Condens. Matter **491**, 79–83 (2016).
[44]M. W. K. Li, G.-D. Zhou, and T. C. W. Mak, *Advanced Structural Inorganic Chemistry* (Oxford University Press, Oxford, 2008).
[45]S. C. Lv, B. Shanmugavelu, Y. P. Wang, Q. N. Mao, Y. J. Zhao, Y. Z. Yu, J. H. Hao, Q. Y. Zhang, J. R. Qiu, and S. F. Zhou, Adv. Opt. Mater. **6**, 1800881 (2018).